ELSEVIER

International Journal of Heat and Fluid Flow 23 (2002) 455–470

International Journal of HEAT AND FLUID FLOW

www.elsevier.com/locate/ijhff

Transition on a flat plate with a semi-circular leading edge under uniform and positive shear free-stream flow

A. Palikaras, K. Yakinthos, A. Goulas *

Department of Mechanical Engineering, Laboratory of Fluid Mechanics & Turbomachinery, Aristotle University of Thessaloniki, 54006 Thessaloniki, Greece

Received 20 August 2001; accepted 26 February 2002

Abstract

The effect of the free-stream velocity profile on the transition from laminar to turbulent flow on a flat plate was studied experimentally and numerically and it is presented in this paper. The flows investigated are based on the T3L test case of the ERCOFTAC Special Investigation Group for transition. According to this test case, the boundary layer development on a flat plate with a semi-circular leading edge is examined by means of transition due to separation, under various free-stream conditions concerning the turbulence intensity and velocity magnitude. In the present work, two free-stream velocity distributions were studied. The first was a uniform velocity one and the second, with a mean shear velocity profile with positive gradient, $\partial\overline{U}/\partial y = 27.7\ \mathrm{s}^{-1}$. Measurements using hot-wire anemometry were taken in two primary regions: far upstream of the flat plate to observe the velocity and turbulence distributions and near the flat plate to capture the boundary layer development and the transition phenomenon. The effect of the two free-stream velocity distributions was studied and it was shown that for both velocity distributions a recirculation region of the flow occurred near the flat plate wall that led to transition dominated by the boundary layer separation. For the positive velocity gradient the separation region was smaller compared to the case of uniform free-stream profile. Both cases were also studied computationally. Two widely used linear eddy-viscosity turbulence models, the k–ε and the k–ω with specific low Reynolds formulations were applied and in addition, a non-linear eddy-viscosity based on the k–ε model has been implemented. In general, all the k–ε models gave satisfactory predictions for both flow cases regarding the predicted velocity distributions, while the k–ω model gave poor results. Concerning the longitudinal Reynolds stress distributions in the near-wall region, the non-linear k–ε model gave the best predictions inside the separation zone but it over predicted the corresponding values beyond the reattachment point while beyond the separation the linear models predicted the longitudinal stresses in a more satisfactory way.

Keywords: Transition; Separation; Turbulence; Mean shear; CFD; Turbulence modeling; k–ε; k–ω; Linear and non-linear eddy-viscosity model

1. Introduction

Transition is a phenomenon of primary interest in the industry of aeronautics and turbomachinery due to the complex behavior of fluid flow and the dramatic change of flow properties, such as skin friction, heat transfer coefficients, pressure distribution, etc. A satisfactory prediction and even better, control of the transitional region can increase the performance of a crucial device. In the past, a large amount of work has been carried out to investigate the conditions under which transition occurs and how these conditions affect its development. Mayle (1991), in his overview on transition, has given a detailed description of the transition phenomenon. By regarding the three essential ways that transition can occur, i.e., natural, by pass and transition through boundary layer separation, it was found that transition is primary affected by the free-stream turbulence (FST) level (Van Driest and Blumer, 1963; Hall and Gibbings, 1972) the pressure gradient, Mayle, (Blair, 1982) and a possible separation of a laminar boundary layer that at reattachment becomes turbulent. For the effect of FST level on transition it has been observed that as the value of FST level increases, the length of the laminar flow region tends to decrease. The FST levels for most cases examined in the past started at very low values, 0.1%

* Corresponding author.

E-mail addresses: apalik@egnatia.ee.auth.gr (A. Palikaras), kyros@eng.auth.gr (K. Yakinthos), goulas@eng.auth.gr (A. Goulas).

0142-727X/02/$ - see front matter
PII: S0142-727X(02)00146-7

Nomenclature

$c_{\varepsilon 1}$, $c_{\varepsilon 2}$	coefficients in ε-equation
$c_{\varepsilon 3}$	vortex stretching parameter in the ε-equation
c_μ	coefficient in eddy-viscosity equation
c_u	correction factor for near wall measurements
c_1–c_5	coefficients in the non-linear Reynolds stresses formulation
$f_{\beta^*} f_\beta$	coefficients in k–ω model.
f_μ	damping function in low Reynolds number turbulence modeling (k–ε model)
k	turbulence kinetic energy
l	dissipation rate length scale in the free-stream region
P_k	production of turbulence energy
$R_t, \tilde{R}_t$	local turbulence Reynolds number ($=k^2/(v\varepsilon), k^2/(v\tilde{\varepsilon})$ resp.)
S_{ij}	strain tensor ($=\partial u_i/\partial x_j + \partial u_j/\partial x_i$)
$S, \tilde{S}$	strain invariants ($=k/\varepsilon\sqrt{S_{ij}S_{ij}/2}, k/\tilde{\varepsilon}\sqrt{S_{ij}S_{ij}/2}$, resp.)
T_u	turbulence level (longitudinal velocity component, x-direction)
τ_w	wall shear stress
u, v	velocity components ix x–y directions
U_c	central velocity
U_e	velocity at the edge of boundary layer, $U_e = 0.995U_{max}$
u_ε	Kolmogorov velocity scale, $u_\varepsilon = (v\varepsilon)^{1/4}$
u_τ	friction velocity, $u_\tau = \sqrt{\tau_w/\rho}$
$\overline{U}$	mean velocity
u^+	dimensionless velocity, $u^+ = \frac{u}{u_\tau}$
u', v', w'	mean values of fluctuations (x, y, z directions)
$\overline{u'^2}$	$=\overline{u'u'}$, Reynolds stresses (x-component)
$\overline{v'^2}$	$=\overline{v'v'}$, Reynolds stresses (y-component)
$\overline{w'^2}$	$=\overline{w'w'}$, Reynolds stresses (z- component)
y^+	dimensionless wall distance, $y^+ = yu_\tau/v$

Greeks

α^*	damping function in low Reynolds number turbulence modeling (k–ω model)
$\alpha, \beta, \beta^*, \sigma, \sigma^*$	coefficients in k–ω model
δ	boundary layer thickness
δ^*	boundary layer displacement thickness
ε	dissipation rate of k
$\tilde{\varepsilon}$	isotropic dissipation rate of k
H	boundary layer shape factor
θ	boundary layer momentum thickness
v	kinematic viscosity
v_t	turbulent kinematic viscosity
ρ	density
τ	dimensionless time
τ_0	dimensionless time (constant offset value of turbulence intensity)
Ω_{ij}	vorticity tensor ($=\partial u_i/\partial x_j - \partial u_j/\partial x_i$)
$\Omega, \tilde{\Omega}$	vorticity invariants ($=k/\varepsilon\sqrt{\Omega_{ij}\Omega_{ij}/2}, k/\tilde{\varepsilon}\sqrt{\Omega_{ij}\Omega_{ij}/2}$, resp.)

where natural transition occurs, and reached values, 2%, 4%, even 10%, where by-pass transition is the main mechanism. In parallel and as a result of the leading edge geometry, there is a possible onset of transition due to boundary layer separation. This separation accelerates transition and combined with the FST affects significantly the transition region. A compilation of detailed experimental and computational data was carried out by ERCOFTAC where a Special Interest Group started the study of transition in 1991. The main interest of the work was on the effects of FST and of the pressure gradient on transition. In parallel, computational simulations were performed using the available integral methods and/or various turbulence models. Savill (1995) presented a collection of the computational contributions for numerous test cases where integral methods and eddy-viscosity models have been tested. In general, both methods gave good agreement with experiments. For the eddy-viscosity models, the Launder–Sharma k–ε model was found to give the best predictions, despite its deficiency to predict adequately flows characterized by the presence of adverse pressure gradient. For the T3L case especially, AUTh group (1994), Yakinthos and Goulas (1999), presented computational results based on the low Reynolds k–ε Launder–Sharma model, and in a good agreement with the experiments of VUB group (1992) for high FST levels and with the experiments of Coupland and Brierley (1996, Rolls-Royce group) for zero and non-zero pressure gradient. For these predictions it was necessary to incorporate the Kato and Launder (1993) modification in the production term of kinetic energy to suppress the spurious generation of k in the impingement region at the stagnation point that led subsequently to smaller separation region than the experimental one. Finally, another approach has been made in the same period by Voke and Yang (1995). They presented excellent computational results for the T3L test case using LES and they concluded that separation occurred under all the free-stream conditions that they have tested followed by transition, even when they started their computations with zero FST.

The majority of test cases examined through the SIG of ERCOFTAC for transition, has focused on flows with isotropic or weakly anisotropic FST with varying intensities and/or the existence of strong favorable/adverse pressure gradient. The experimental results that

will be presented here, fill a gap in research on transition since the same T3L case is studied by having as a free-stream condition a strongly anisotropic turbulence with large turbulence intensity in comparison with the original test case.

The question posed is whether there is a direct effect of mean velocity shear on transition and particularly in the case of transition induced by boundary layer separation. The present work therefore, comes to answer this by comparing the velocity profiles in the region of transition for a uniform and a mean shear inlet velocity profile, which in the region of the leading edge have the same turbulence intensity.

The typical development of isotropic FST with distance along a wind tunnel is a decaying function including fixed constants to match the tunnel's characteristics, Tenekes and Lumley (1985). Various formulations for the FST decay in a wind tunnel have been used in the past. Among them is an exponential equation, provided by Baines and Peterson (1951), which predicts a FST development that starts form high levels of turbulence generated mostly by the turbulence grid generator and reaches, in an asymptotic way, to the zero value.

Champagne et al. (1970) studied experimentally the behavior of pure shear flows with $\partial\overline{U}/\partial y > 0$ in tunnel flows. Their primary conclusion was that for a free shear with a nearly homogeneous turbulence, a growth of turbulence level downstream is observed. Harris et al. (1977) presented further experiments with higher shear values in larger values of dimensionless time $\tau = x/U_c(\partial\overline{U}/\partial y)$ (a parameter that combines the distance downstream the flow development with the value of shear gradient and the centre-line velocity U_c), where the downstream turbulence growth was very clear. Furthermore, Rohr et al. (1988) investigated the growth of turbulence in a uniform mean shear flow by carrying out experiments in a water tunnel. It was again observed, that by keeping a nearly homogeneous turbulence, the longitudinal turbulence intensity $u'/\overline{U}$ plotted against dimensionless downstream distance x (non-dimensionalised by the channel height) or against the dimensionless development time τ, was increasing for various initial conditions and length scales. Tavoularis and Corrsin (1981) have also carried out experiments in nearly homogeneous shear flow. They presented the downstream development of the turbulence component energies $\overline{u'u'}/U_c^2$, $\overline{v'v'}/U_c^2$, $\overline{w'w'}/U_c^2$ which increased in a monotonic way. On the basis of the above, there was an effort in this work to combine the characteristics and laws governing pure shear channel flows with the T3L test case. A mean shear inlet velocity distribution was imposed and a comparison with the experiments for the original T3L test case was carried out.

The present work is divided in two parts. In the first part, detailed measurements of the velocity distribution and onset of transition through boundary layer separation in the region of the wall of the flat plate for both uniform and mean shear velocity inlet distributions are presented. In the second part two linear eddy-viscosity turbulence models and one non-linear eddy-viscosity model were used to predict the flow in an effort to examine their behaviour under such flow conditions.

2. Experimental setup

The experiments were carried out in a wind tunnel at the Laboratory of Fluid Mechanics & Turbomachinery at the Aristotle University of Thessaloniki (LFMT-AUTh). It is an open wind tunnel with a cross section of 307×307 mm^2 and a test section 1 m long. Indicative velocity measurements in the spanwise direction have shown that the blockage effect due to the wind tunnel's side walls was negligible. The measured velocities have been carried out in the upper surface of the plate. The total length of the wind tunnel is 9 m and the air is driven by an axial fan. The boundary layer under study was developing on a flat plate 1 m long, 300 mm wide and 10 mm thick made of aluminium, with a semi-circular leading edge with 10 mm diameter, which blends smoothly to the flat portion. This is chosen to match the T3L case. The entire arrangement is illustrated in Fig. 1 where also the co-ordinate system used is shown.

In the case of uniform inlet velocity the required turbulence level is produced by a turbulence generator, placed at an appropriate distance upstream of the flat plate. The resultant turbulence has been found to be weakly anisotropic with an intensity of the longitudinal velocity fluctuation $T_u = 7\%$. The turbulence generator used is a rectangular grid made of 6 mm square bars. The open ratio is approximately 60%. Table 1 summarizes the measurement positions. $(x, y) = (0, 0)$ refers to the stagnation line in the leading edge.

The shear generator used in the experiments is similar to the ones reported by Champagne et al. (1970), Harris et al. (1977), Rohr et al. (1988), Tavoularis et al. and consists of screens with various grid sizes and solidities. The wind tunnel in the vertical direction is divided to 15 sections using a 2 mm thick aluminium plates. A combination of screens is used to introduce different resistance to the flow in each of the 15 sections and thus downstream of the generator, a velocity profile with a

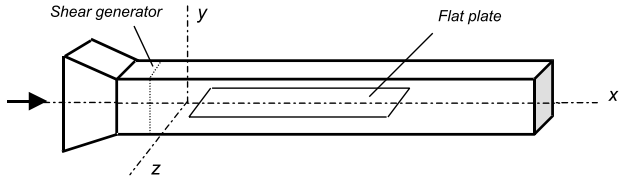

Fig. 1. Wind tunnel and flat plate arrangement. System of coordinates.

Table 1
Measurement positions

X (m)	Y (m)	Z (m)	
−0.150	From −0.150 to +0.150	0	Detailed inlet velocity and turbulence distributions with x-wire for uniform and sheared mean velocity profile
From −0.150 to +0.8	$Y = 0.075$	0	Free-stream velocity and turbulence distributions to observe the behaviour of these quantities in presence and absence of shear. x-wire measurements
From +0.006 to +0.03	From flat plate's wall up to $y = 0.05$ in normal direction. First point from the wall located at $y = 0.0003$	0	Detailed velocity measurements in the boundary layer. Single hot-wire

mean shear is produced. The turbulence level of the longitudinal velocity component, measured at 100 mm upstream the leading edge and in the center-line is approximately $T_u = 7\%$. When the velocity at the axis of the wind tunnel to the leading edge is $U_c = 5$ m/s, the mean velocity gradient in the vertical direction in the core region of the tunnel is equal to $\partial\overline{U}/\partial y = 27.7\ s^{-1}$. For both cases the Reynolds number based on the plate thickness is 3300. The measurements reported here were carried out using a constant temperature anemometer (DISA 55M01). Two types of hot-wire probes were used: a single wire for the measurements near the flat plate and a x-wire for measurements in the free-stream region. A traverse mechanism capable of moving a probe 200 mm, both in the streamwise direction and in the direction normal to the upper flat plate surface was used. The accuracy of the movement in each of the two directions was 0.01 mm. The hot-wire signal was stored in a computer. A 16-bit A/D card capable of sampling simultaneously up to four channels was used. The acquisition frequency was 5 KHz. For each measurement point, 125,000 discreet values were taken for a time period of 25 s.

3. Error analysis

All hot-wire probes were calibrated in the free-stream against a Pitot-Static tube every hour of use, to avoid drifting due to ambient temperature variations or other factors. In this way the error in the velocity reading was approximately 1%. Another reason for errors in velocity, which was examined, was the heat losses while the sensor was very close to the aluminium flat plate surface. Lange et al. (1999) investigated this error and proposed relationships in order to correct the velocity signal. According to their work, the correction factor $c_u = U_{real}/U_{measured}$ can be calculated from a simple equation.

$$c_u = 1.0 - \exp(-0.4y^{+^2}), \tag{1}$$

where, y^+ is the normalized y distance in wall units, $y^+ = yu_\tau/v$. In the present experiment, the first measurement position was at $y = 0.3$ mm for all measurement stations in x-axis. The value of $y = 0.3$ mm corresponded to $y^+ = 5$ at the first measurements stations in x-axis. Downstream this location, y^+ had values higher than 5. The above equation, for $y^+ = 5$ gives $c_u = 0.99995$, which means that there is no need to correct for heat losses. The quantity y^+ used in the equation can be calculated if the wall shear stress is known. The way that the wall shear stress has been calculated will be described below.

4. Experimental results

4.1. Wind tunnel characteristics

4.1.1. Uniform inlet profile

The distribution of the free-stream longitudinal turbulence intensity generated by the turbulence generator, together with the empirical correlation developed by Baines and Peterson, for isotropic grid-generated turbulence, is presented in Fig. 2(a).

The empirical correlation between the FST T_u, the bar width, b, and the distance from the turbulence generating grid, l, is:

$$T_u = 1.12\left(\frac{l}{b}\right)^{-5/7}. \tag{2}$$

If the measured longitudinal turbulence intensity is in agreement with the above empirical expression, then there is an indication that the turbulence is isotropic. Upstream of the plate there is a difference between the experimental results and the empirical correlation, which becomes smaller downstream. The flow at the first stations is non-isotropic and tends to an almost isotropic behavior far downstream. This is supported by the distribution of the mean values of Reynolds stresses $\overline{u'u'}$ and $\overline{v'v'}$ for the same x and y positions as shown in Fig. 2(b). There is a difference between these quantities at the first stations, which downstream becomes smaller. According also to Bradshaw (1971), it is very difficult to obtain an isotropic turbulence in the near region behind a turbulence generation grid. Usually the ratio of the $\overline{u'u'}$ and $\overline{v'v'}$ is equal to 0.75, i.e., $\overline{v'v'} = 0.75\overline{u'u'}$ and downstream the grid, the turbulence returns slowly to isotropic. For the present experiment in the region behind the grid, it was also found that $\overline{v'v'}$ was equal to $0.75\overline{u'u'}$.

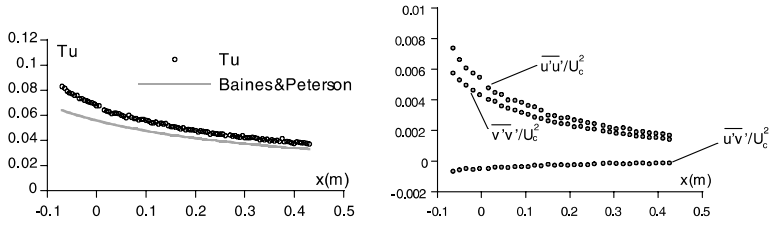

Fig. 2. (a) Comparison of the longitudinal turbulence distribution, in the streamwise direction at a normal distance $y = 75$ mm from the plate, with the empirical correlation of Baines and Peterson. (b) Reynolds stresses distribution downstream the fluid flow at the same distance.

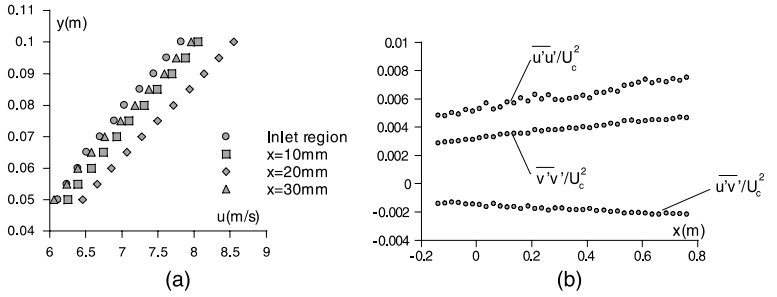

Fig. 3. (a) The velocity gradient away from the plate surface for various stations in x-axis. (b) Distribution of the Reynolds stresses in the streamwise direction at a normal distance $y = 75$ mm form the plate.

4.1.2. Positive mean shear inlet profile

The mean velocity profile at the inlet of the test section (at a distance 150 mm upstream of the leading edge) had a positive gradient with $\partial\overline{U}/\partial y = 27.7\ \mathrm{s}^{-1}$ and a velocity at the middle of the wind tunnel height, $U_c = 5$ m/s. Measurements at various stations on the flat plate and far from the surface ($y = 50$–100 mm) showed that the velocity gradient $\partial\overline{U}/\partial y$ remained almost constant and equal with the gradient at the inlet region as presented in Fig. 3(a).

The normal Reynolds stresses increase in the downstream direction as shown in Fig. 3(b). Also, Rohr et al. demonstrated that the growth of turbulence in a uniform mean shear flow occurs nearly at the same rate regardless of the shear or the mean centerline velocity when the growth is measured in terms of the dimensionless time $\tau = x/U_c(\partial\overline{U}/\partial y)$. The turbulence intensity growth for the range of $\tau = 5$–25 investigated in his experiment is given by the following relation:

$$\frac{u'}{\overline{U}} = C_1\left(\frac{x}{U_c}\frac{\partial\overline{U}}{\partial y} - \frac{x_0}{U_c}\frac{\partial\overline{U}}{\partial y}\right) = C_1(\tau - \tau_0), \tag{3}$$

where x_0 is a function of the size of the initial disturbance and C_1 is a constant independent of x but may depend on the facility. In our experiment C_1 was taken equal to unity, since there is no an exact formula to calculate this coefficient. Using the dimensionless time, the range of in the present measurements was found to be $\tau = 10$–16. The corresponding plot of the turbulence intensity $u'/\overline{U}$ versus the dimensionless time is presented in Fig. 4 where the present experimental data are shown with full circles.

A very good agreement between the current measurements and the measurements in the wind tunnel of Tavoularis & Corrsin and Rohr's expression is shown.

Fig. 5 shows the distributions for both cases of the longitudinal normal Reynolds stresses in the free-stream above the boundary layer in the x-direction and in the region of the flow evolution. It can be seen very clearly that the longitudinal Reynolds stresses, have the same values for both cases.

4.2. Flow development

On the above wind tunnel measurements for the flat plate took place.

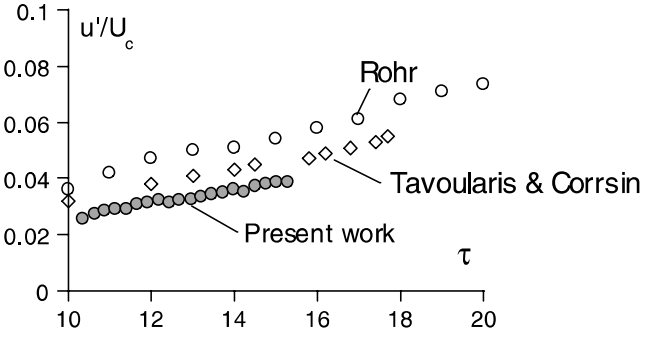

Fig. 4. Distribution of the longitudinal turbulence intensity, $\overline{u'}/U$, as a function of the dimensionless time τ.

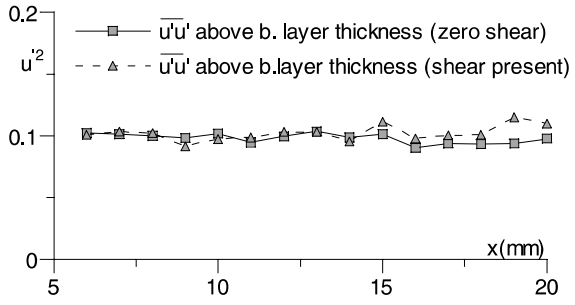

Fig. 5. Downstream evolution of $\overline{u'u'}$ stresses above the boundary layer for both cases.

4.2.1. Transition under uniform inlet profile

Mean-velocity profiles within the boundary layer to determine the transition region were acquired. All boundary layer profiles were obtained at the centre of the test surface in the spanwise direction. The first measurement position in the streamwise direction was set at $x = 6$ mm and in the axis normal to the flat plate's surface at $y = 0.3$ mm for all x-positions. The step of the measured velocity profiles in the streamwise direction was 1 mm. The measured velocities within the boundary layer, is normalized by the maximum velocity $U_{\max}$, measured at each station. The distance y has been normalized by the height H of the wind tunnel. The distance y at which, the velocity inside the boundary layer attained the value $0.995U_{\max}$ at each measurement station was assumed to be the boundary layer thickness. In Fig. 6, the boundary layer velocity profiles at five stations are given.

The velocity profiles at $x = 6$, 11 and 12 mm have the typical shape of a separated boundary layer. This is indicated also by extrapolating the experimental data towards the wall. The region between $y = 0$ mm (flat plate surface) and $y = 0.3$ mm can be simulated by a second order polynomial. The coefficients of the polynomial equation can be calculated by using the following conditions: $u_{y=0\ \mathrm{mm}} = 0$ m/s, $u_{y=0.3\ \mathrm{mm}}$ equals to the velocity measured at $y = 0.3$ mm for each station in streamwise direction and $\mathrm{d}u/\mathrm{d}y|_{y=0.3\ \mathrm{mm}}$ is calculated from the measured values of velocity at $y = 0.3$ and 0.4 mm at each measurement station. Applying the above extrapolation, the existence of a separation bubble even in the first measurement station, located at $x = 6$ mm can be observed. At $x = 17$ mm the extrapolation indicates an attached boundary layer. The data from the above extrapolation were also used for the calculation of the wall shear stress in the region where a separation bubble was indicated by calculating the velocity derivative close to the wall. In the region where an attached boundary layer was indicated, the momentum integral equation was used for the calculation of the wall shear stress as it will be mentioned below. In Fig. 7, the RMS profiles (root mean square value of fluctuations), at five stations in the x-direction are given. The position in y-direction corresponding to the maximum value of RMS at each station x, as well as the maximum value of RMS inside the boundary layer at each measurement station are given in Fig. 8. The typical RMS profile in the y-direction shows a maximum value at some distance from the wall, marking the position of maximum shear and the

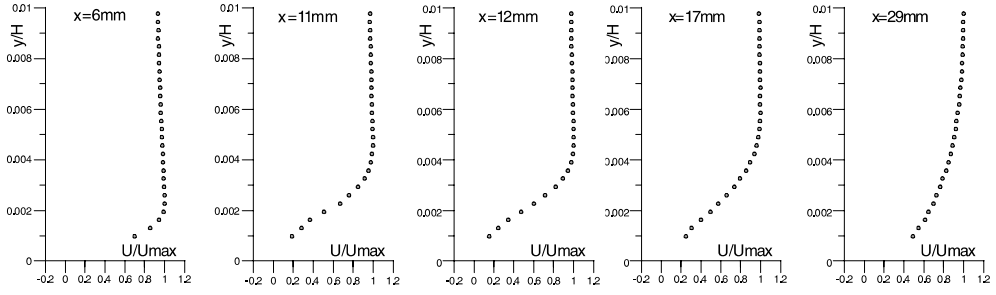

Fig. 6. Uniform inlet velocity distribution. Boundary layer velocity profiles at five stations.

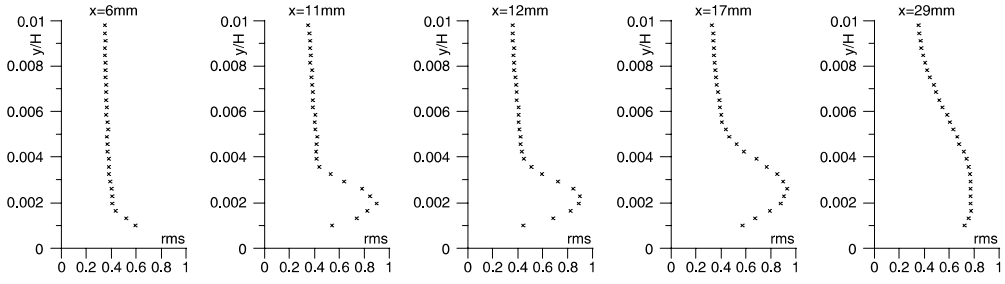

Fig. 7. Uniform mean inlet velocity distribution. Boundary layer RMS profiles at five stations.

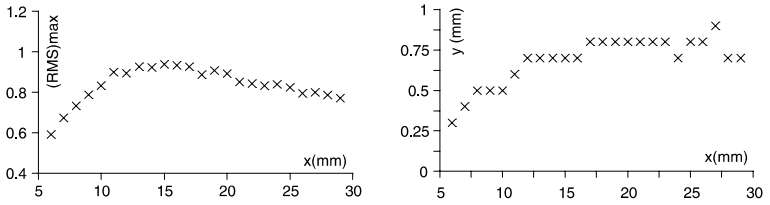

Fig. 8. Uniform inlet velocity distribution. Maximum value of RMS and the corresponding position at y-axis, inside the boundary layer.

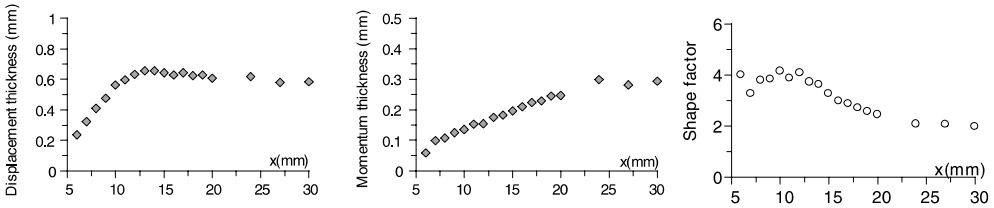

Fig. 9. Uniform inlet velocity distribution. Boundary layer integral parameters for uniform inlet velocity profile.

edge of the recirculation bubble, and then drops asymptotically to the corresponding free-stream value.

In Fig. 8(a), the maximum value of RMS increases from the first measurement station, attains the maximum value at $x = 12$ mm remains constant until $x = 17$ mm and then begins to decrease. In Fig. 9, the integral parameters, displacement thickness, momentum thickness and the shape factor of the boundary layer as a function of distance from the leading edge are presented. For the calculation of the parameters, in the region between $y = 0$ and 0.3 mm the extrapolated data were used. In this way, the resultant diagram for the shape factor is qualitatively right although the values are lower than that found in to similar experiments.

According to Ellsworth and Mueller (1991), the shape factor H of a separated boundary layer has its peak at the beginning of transition. From Fig. 9, the position where the shape factor has maximum value is at $x = 12$ mm. Downstream, the shape factor decreases and in the last stations where the boundary layer is attached reaches a value, approximately of 2, which is far from the empirical value 1.3–1.4 of a fully turbulent boundary layer. This is due to the fact that the boundary layer in the region has not yet become fully turbulent. The displacement thickness has also a maximum value at the position $x = 12$ mm. An alternative method to understand if an attached boundary layer (downstream of the position $x = 17$ mm) is a developing or a fully turbulent one, is to compare the experimental measurements, with Musker (1979) expression in wall units for the velocity distribution given as:

$$u^+ = 5.424 \tan^{-1}\left[\frac{(2y^+ - 8.15)}{16.7}\right] + \log_{10}\left[\frac{(y^+ + 10.6)^{9.6}}{(y^{+2} - 8.15y^+ + 86)^2}\right] - 3.52, \quad (4)$$

where, $y^+ = (y \cdot u_\tau)/v$, $u^+ = u/u_\tau$, u_τ is friction velocity, $u_\tau = \sqrt{\tau_w/\rho}$, τ_w is the wall shear stress.

For a flat plate at zero incidence the shear stress on the wall is given as:

$$\frac{\tau_w}{\rho} = U_e^2 \frac{d\vartheta}{dx}, \quad (5)$$

where ϑ is the momentum thickness. Given the experimental momentum thickness distribution, Fig. 9, τ_w can be calculated from the above expression. In Fig. 10 the calculated values of u^+ based on the experimental data together with those obtained from Musker's expression, are given.

The difference between the experimental data and the theoretical expression reinforces the above conclusion that downstream the reattachment point the boundary layer is not yet fully turbulent.

At $x = 17$ mm (Fig. 10), only the first two points follow Musker's expression ($y^+ < 10$). In the range of y^+ $20 < y^+ < 1000$, u^+ decreases relatively fast. Downstream of the position $x = 17$ mm more and more points fit Musker's expression. At $x = 29$ mm (Fig. 11) the experimental velocity profile is the same with Musker's profile until a y^+ approximately equal to 80 and then decreases with a much slower rate than that at $x = 17$ mm. At $x = 29$ mm, the Reynolds number based on momentum thickness attains a value of 110 which is far below the value 320 at which according to Murlis et al. (1982) turbulent boundary layer can be maintained. The shape factor has a value approximately of 2 and the boundary layer seems to attain gradually the shape of a fully developed turbulent boundary layer.

4.2.2. Transition under mean shear inlet velocity profile

Velocity profiles at various stations are presented in Fig. 12. These velocity profiles are also in the

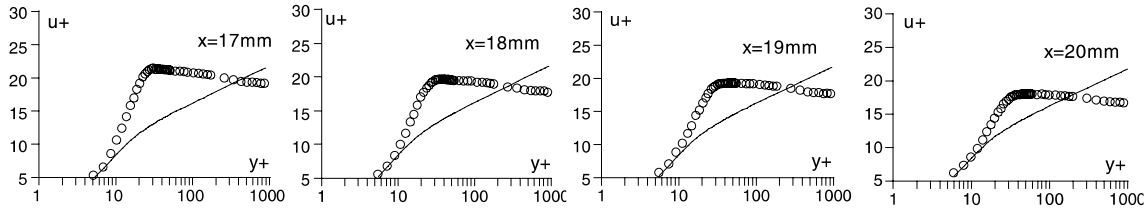

Fig. 10. Comparative diagrams of Musker's profile and experimental measurements, within the boundary layer at the first stations downstream of the reattachment point, for uniform inlet velocity profile.

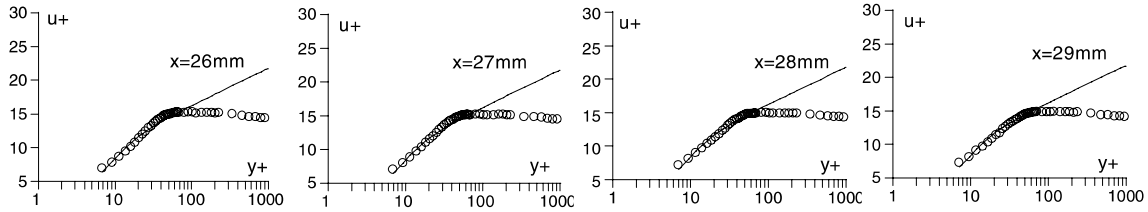

Fig. 11. Comparative diagrams of Musker's profile and experimental measurements, within the boundary layer at the last stations downstream of the reattachment point, for uniform inlet velocity profile.

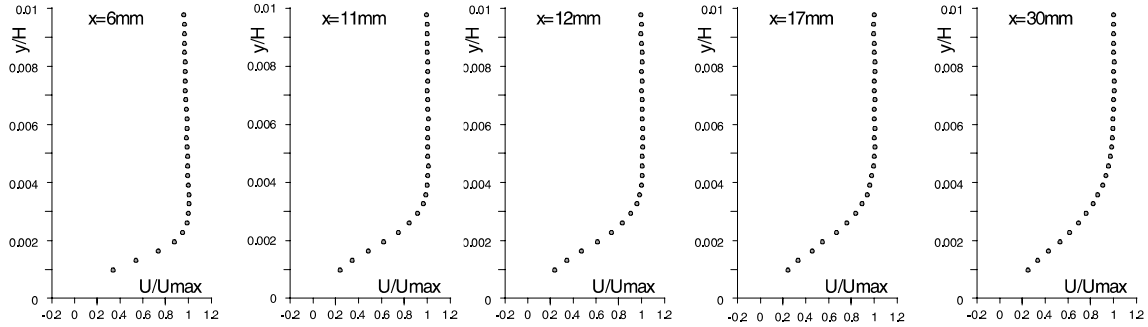

Fig. 12. Mean shear inlet velocity distribution. Boundary layer velocity profiles at various stations.

dimensionless form of $(U/U_{\max}) = f(y/H)$, where H is the wind tunnel height, but there were changes in the way that the maximum velocity and boundary layer thickness were defined. The value y, of the measurements within the boundary layer, where the velocity gradient becomes equal to 0.995 of the velocity gradient in the free-stream, was defined as the edge of the boundary layer. The corresponding velocity value at the same y was taken as the $U_{\max}$.

Applying the same extrapolation procedure, as in the case of uniform inlet velocity profile, there is an indication of a separating boundary layer from the first measurement station of $x = 6$ mm. The same procedure indicated that the reattachment point should be located about at $x = 15$–16 mm. The RMS profiles within the boundary layer have the same shape as in the uniform case, Fig. 13. In Fig. 14 the maximum values of RMS at every station in the x-direction are plotted. The peak of $(\mathrm{RMS})_{\max}$ is at $x = 15$–16 mm and at $y = 0.7$ mm above the plate. Downstream of this position the value of RMS is a little smaller and remains almost constant until the last station.

The displacement thickness and the momentum thickness in this case calculated as mentioned above are shown in Fig. 15. In the region $y = 0$–0.3 mm again the extrapolated data was taken into account.

From $x = 7$–9 mm the shape factor remains constant and equal to the maximum value. Downstream of $x = 9$ mm H begins to decrease slowly until the position $x = 15$ mm. The region from $y = 0$ mm to $y = 0.3$ mm is where the reverse flows probably exists. Downstream of $x = 15$ mm the shape factor decreases quickly until $x = 20$ mm, and remains almost constant.

5. Computational analysis

5.1. Mathematical formulation

In order to understand the physics of the experimentally investigated flows, CFD work was carried out.

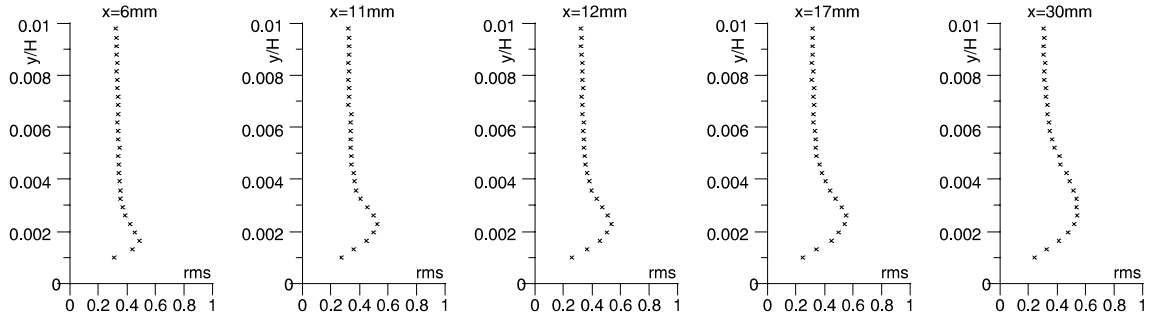

Fig. 13. Mean shear inlet velocity distribution. RMS profiles within the boundary layer at various stations x.

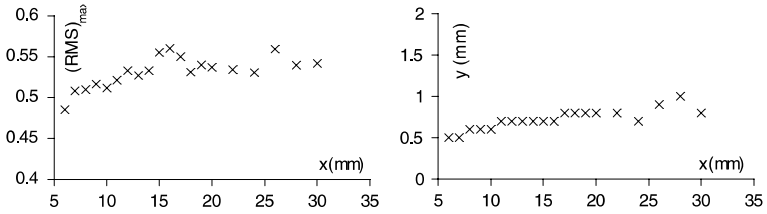

Fig. 14. Mean shear inlet velocity distribution. Plots of the maximum value of RMS and the corresponding position at y-axis, inside the boundary layer.

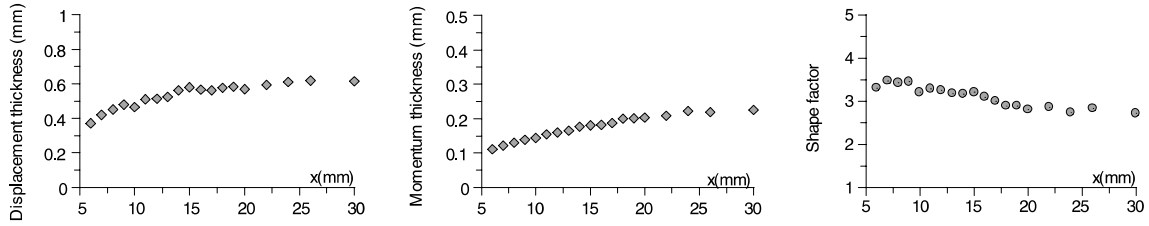

Fig. 15. Mean shear inlet velocity distribution. Boundary layer integral parameters for mean shear velocity profile.

The Navier–Stokes governing the fluid flow in their two-dimensional tensorial form are given below:

$$\frac{\partial \overline{U_i}}{\partial x_i} = 0, \tag{6}$$

$$\overline{U_j}\frac{\partial \overline{U_i}}{\partial x_j} = -\frac{1}{\rho}\frac{\partial \overline{p}}{\partial x_i} + \frac{\partial}{\partial x_j}\left[\nu\left(\frac{\partial \overline{U_i}}{\partial x_j} + \frac{\partial \overline{U_j}}{\partial x_i}\right) - \overline{u_i' u_j'}\right]. \tag{7}$$

To model the turbulence of the flow, three models were used. The first two models are using the isotropic Boussinesq's hypothesis for the Reynolds stresses tensor, i.e. $-\overline{u_i' u_j'} = 2\nu_t S_{ij} - 2/3 k\delta_{ij}$, with S_{ij} the mean strain-rate tensor and ν_t the eddy-viscosity calculated with appropriate formulations depending on the model. The first linear eddy-viscosity model is based on the k–ε formulation with the low Reynolds modifications after Abe et al. (1994). One advantage of this model is that the Kolmogorov velocity scale u_ε is used for the calculation of y^*, instead of the friction velocity u_τ that is used for the calculation of y^+, which does not become zero either at the separating or at the reattaching points so there are no singularities in the calculation. The second linear model is the k–ω model with the appropriate low Reynolds modifications as introduced by Wilcox (1998). This model was chosen to examine the behavior of this alternative representation of the second closure equation in a turbulence modeling procedure which has been widely used. The transport equations for the two models are given below.

5.1.1. k–ε model

$$\nu_t = c_\mu f_\mu \frac{k^2}{\varepsilon}, \tag{8}$$

$$\overline{U_j}\frac{\partial k}{\partial x_j} = \frac{\partial}{\partial x_j}\left[\left(\nu + \frac{\nu_t}{\sigma_k}\right)\frac{\partial k}{\partial x_j}\right] - \overline{u_i' u_j'}\frac{\partial \overline{U_i}}{\partial x_j} - \varepsilon, \tag{9}$$

$$\overline{U_j}\frac{\partial \varepsilon}{\partial x_j} = \frac{\partial}{\partial x_j}\left[\left(\nu + \frac{\nu_t}{\sigma_\varepsilon}\right)\frac{\partial \varepsilon}{\partial x_j}\right] - C_{\varepsilon 1}\frac{\varepsilon}{k}\overline{u_i' u_j'}\frac{\partial \overline{U_i}}{\partial x_j} - C_{\varepsilon 2} f_\varepsilon \frac{\varepsilon^2}{k}, \tag{10}$$

$$f_\varepsilon = \left[1 - \exp\left(-\frac{y^*}{3.1}\right)\right]^2 \left\{1 - 0.3\exp\left[-\left(\frac{R_t}{6.5}\right)^2\right]\right\},$$
$$f_\mu = \left[1 - \exp\left(-\frac{y^*}{14}\right)\right]^2 \left\{1 + \frac{5}{R_t^{3/4}}\exp\left[-\left(\frac{R_t}{200}\right)^2\right]\right\}, \tag{11}$$

with $\sigma_k = 1.4$, $\sigma_\varepsilon = 1.4$, $C\varepsilon 1 = 1.5$, $C_{\varepsilon 2} = 1.9$, $c_\mu = 0.09$.

5.1.2. k–ω model

$$\nu_t = \alpha^* \frac{k}{\omega}, \tag{12}$$

$$\overline{U_j}\frac{\partial k}{\partial x_j} = \frac{\partial}{\partial x_j}\left[(\nu + \sigma^*\nu_t)\frac{\partial k}{\partial x_j}\right] - \beta^* k\omega - \overline{u_i'u_j'}\frac{\partial \overline{U_i}}{\partial x_j}, \tag{13}$$

$$\overline{U_j}\frac{\partial \omega}{\partial x_j} = \frac{\partial}{\partial x_j}\left[(\nu + \sigma\nu_t)\frac{\partial \omega}{\partial x_j}\right] - \beta\omega^2 - \alpha\frac{\omega}{k}\overline{u_i'u_j'}\frac{\partial \overline{U_i}}{\partial x_j}, \tag{14}$$

$$\alpha^* = \frac{\alpha_0^* + Re_t/R_k}{1 + Re_t/R_k},$$
$$\alpha = \frac{13}{25}\frac{\alpha_0 + Re_t/R_\omega}{1 + Re_t/R_\omega}(\alpha^*)^{-1}, \tag{15}$$
$$\beta^* = \frac{9}{100}\frac{4/15 + (Re_t/R_\beta)^4}{1 + (\mathrm{Re}_t/R_\beta)^4}f_{\beta^*},$$

with $\beta = \frac{9}{125}f_\beta$, $\sigma^* = \sigma = 0.5$, $\alpha_0^* = \frac{1}{3}\beta_0$, $\alpha_0 = \frac{1}{9}$, $R_\beta = 8$, $R_k = 6$, $R_\omega = 2.95$, $\beta_0 = \frac{9}{125}$ and $f_\beta = (1 + 70\chi_\omega)/(1 + 80\chi_\omega)$, $\chi_\omega = \left|(\Omega_{ij}\Omega_{jk}S_{ki})/(\beta_0^*\omega)^3\right|$, $f_\beta^* = 1$, $\chi_k \leqslant 0$, $f_\beta^* = (1 + 680\chi_k^2)/(1 + 400\chi_k^2)$, $\chi_k > 0$ with $\chi_k = (1/\omega^3)(\partial k/\partial x_j)(\partial\omega/\partial x_j)$.

It is well known that turbulence models based on Boussinesq's hypothesis suffer from some important weaknesses primary focused on the inability to capture the Reynolds stress anisotropy and on the excessive abnormal generation of turbulence in regions near stagnation points. To eliminate the second weakness, Kato and Launder proposed a different formulation of the production term in the k-equation, $P_k = f_\mu C_\mu \varepsilon S\Omega$, instead of its original formulation, i.e., $P_k = f_\mu C_\mu \varepsilon S^2$. This modification has been used by Yakinthos and Goulas (1995, 1999) for similar test cases with stagnation point at the leading edge of flat plates but it was found that for flows dominated by a separated boundary layer, it led to larger recirculation regions. Tsuchiya et al. (1997), in a more theoretical basis, proved that the Kato and Launder modification has an inconsistency in the modeling of Reynolds stresses, where it only revises the expression of P_k in the equation of k while it uses the conventional approximation of $-\overline{u_i'u_j'}$ in the momentum equation. A new modification therefore was proposed and was used in the present work, as follows:

$$P_k = -\overline{u_i'u_j'}\frac{\partial \overline{U_i}}{\partial x_j} = f_\mu C_\mu^* \varepsilon S^2, \quad \nu_t = f_\mu C_\mu^* \frac{k^2}{\varepsilon},$$
$$C_\mu^* = C_\mu \frac{\Omega}{S} \quad \left(\frac{\Omega}{S} < 1\right), \quad C_\mu^* = C_\mu \quad \left(\frac{\Omega}{S} \geqslant 1\right). \tag{16}$$

For the reasons described above and in relation that the second experimental case is dominated by the presence of a mean shear that introduces an anisotropy to the flow, a third non-linear eddy-viscosity turbulence model was also used. The chosen model was that introduced in a final version by Craft et al. (1997) in its low Reynolds formulation using two transport equations for k and ε. The equation for the Reynolds stress can be written as follows:

$$\begin{aligned}\frac{\overline{u_i'u_j'}}{k} = {} & \frac{2}{3}\delta_{ij} - \frac{\nu_t}{k}S_{ij} + c_1\frac{\nu_t}{\tilde{\varepsilon}}\left(S_{ik}S_{kj} - \frac{1}{3}\delta_{ij}S_{kl}S_{kl}\right) \\ & + c_2\frac{\nu_t}{\tilde{\varepsilon}}\left(\Omega_{ik}S_{kj} + \Omega_{jk}S_{ki}\right) + c_3\frac{\nu_t}{\tilde{\varepsilon}}\left(\Omega_{ik}\Omega_{jk}\right. \\ & \left. - \frac{1}{3}\delta_{ij}\Omega_{kl}\Omega_{kl}\right) + c_4\frac{\nu_t k}{\tilde{\varepsilon}^2}\left(S_{ki}\Omega_{lj} + S_{kj}\Omega_{li}\right)S_{kl} \\ & + c_5\frac{\nu_t k}{\tilde{\varepsilon}^2}(S_{kl}S_{kl} - \Omega_{kl}\Omega_{kl})S_{ij},\end{aligned} \tag{17}$$

where the eddy-viscosity, turbulence energy and rate of homogeneous dissipation are obtained by the following equations:

$$\nu_t = c_\mu f_\mu \frac{k^2}{\tilde{\varepsilon}}, \tag{18}$$

$$\tilde{\varepsilon} = \varepsilon - 2\nu\left(\frac{\partial\sqrt{k}}{\partial x_i}\right)^2, \tag{19}$$

$$\frac{\partial u_i k}{\partial x_i} = \frac{\partial}{\partial x_i}\left[\left(\nu + \frac{\nu_t}{\sigma_k}\right)\frac{\partial k}{\partial x_i}\right] + P_k - \varepsilon, \tag{20}$$

$$\frac{\partial u_i \tilde{\varepsilon}}{\partial x_i} = \frac{\partial}{\partial x_i}\left[\left(\nu + \frac{\nu_t}{\sigma_\varepsilon}\right)\frac{\partial \tilde{\varepsilon}}{\partial x_i}\right] + \frac{\tilde{\varepsilon}}{k}(c_{\varepsilon 1}P_k - c_{\varepsilon 2}\tilde{\varepsilon}) + E, \tag{21}$$

with the functions appearing in these equations having the expressions

$$c_\mu = \frac{0.3[1 - \exp\{-0.36/\exp[-0.75\max(\tilde{S},\tilde{\Omega})]\}]}{1 + 0.35\left\{\max(\tilde{S},\tilde{\Omega})\right\}^{1.5}},$$
$$f_\mu = 1 - \exp\left\{-\left(\frac{\tilde{R}_t}{90}\right)^{0.5} - \left(\frac{\tilde{R}_t}{400}\right)^2\right\}$$
$$E = 0.0022\frac{\tilde{S}\nu_t k^2}{\tilde{\varepsilon}}\left(\frac{\partial^2 u_i}{\partial x_j \partial x_k}\right)^2,$$
$$c_{\varepsilon 2} = 1.92[1 - 0.3\exp(-\tilde{R}_t^2)]$$

The coefficients in the Reynolds stress tensor have the following values: $c_1 = -0.1$, $c_2 = 0.1$, $c_3 = 0.26$, $c_4 = -10c_\mu^2$, $c_5 = -5c_\mu^2$.

This model has been extensively tested and modified. Chen et al. (1998a) also have tested and compared this model with a three equation non-linear eddy-viscosity model in transitional boundary layers for turbomachine aerodynamics and for flow around highly loaded compressor cascade blades (1998b). In general a good agreement with the experimental data in cases where separation occurred concerning the velocity profiles in regions such as recirculation zones and wake was reported. This two equation model predicted also in a satisfactory way the $\overline{u'u'}$ distributions in selected locations although that the extended version of the three equations model gave better results. The latter, in some cases failed to convergence and numerical instabilities have been observed by the researchers. This was the primary reason for choosing in this work the two equation model since the aim was not a numerical investigation of the non-linear models but their application in order to achieve a better understanding of the flows investigated experimentally.

5.2. The grid used

A full and integrated simulation of the flow using an O-type grid with 150×500 computational nodes was utilized. The topology of the O-type grid used in this work is described by the rectangular west external boundary corresponding to the inlet, wind tunnel walls and outlet regions, the east boundary corresponding to the flat plate's surface and the south and north internal grid lines forming the connection region to close the O-type topology. The inlet region (part of west boundary) and the exit region (also part of west boundary) were placed respectively far upstream and downstream of the leading and trailing edge of the plate. For most of the cells an expansion ratio equal to 1.2 in both x and y directions has been adopted. Preliminary numerical experiments to test for grid dependency were made and it was concluded that the grid used gave a grid independent solution. It must be noted that for low Reynolds k–ε modeling, grid dependency studies are restricted by the parameters of grid distribution near the wall, since some restrictions for the first point near the wall are necessary to have the appropriate boundary conditions for reproducing correctly the near-wall limiting behavior. To be able to simulate accurately the boundary layer evolution, at least 25 grid-points were inside the boundary layer and at least 15 points were located in the region with $y^+ < 10$. Fig. 16 shows details of the grid used near the inlet and the leading edge regions.

5.3. Numerical procedure

A 2-D Navier–Stokes elliptic solver in generalized curvilinear coordinates was used. The control volume technique has been adopted and the coupling of the continuity equation with the momentum transfer equations was made using the pressure correction technique. The primary solved variables are stored in the cell centers of the computational grid and thus the momentum interpolation technique (Rhie and Chow, 1983) was used. The HLPA scheme after Zhu (1991), was introduced for the interpolation of the convective terms and all transport equations were solved to a second order accuracy after also the observations of Chen et al. (1998b). The choice of this scheme was based on the good and stable convergence behavior, which in combination with the second order of accuracy, gives quite satisfactory results, Yakinthos et al. (1995). The solution procedure was based on an under-relaxation procedure after Majumdar (1988), to obtain results independent from the values of the under-relaxation factors. Typical values for under-relaxation values were 0.7 for the primary cartesian velocities while for p, k, ε or ω we used 0.2. Convergence occurred when the maximum normalized residual for all the solved variables was less than 1.E–04.

5.4. Boundary conditions

One major step in simulating fluid flows with a turbulence model is the choice of appropriate inlet values of the solved primary variables u, v, k, ε, or ω for the flow entering the computational domain. For the values of k,

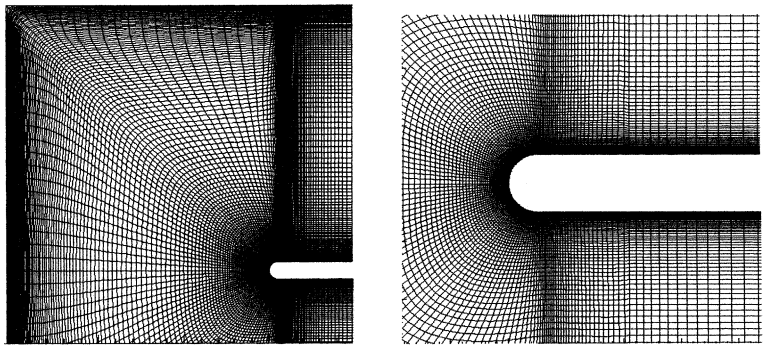

Fig. 16. Partial views of the grid used in the present work. Upper-left area at inlet, leading edge area.

the essential formula based on the turbulence level was, used, i.e. $k = 1.5\ (T_u U)^2$, where T_u is the measured turbulence level for each y station in the wind tunnel's inlet region and U is the corresponding measured velocity. An interpolation of the experimental data was made in order to have the appropriate values for the grid used. The inlet values for ε_0 were obtained using the formula $\varepsilon = k^{3/2}/l$ and for ω_0 using the formula $\omega = \sqrt{k}/l$, where l is the characteristic dissipation rate length scale of turbulence. The length scale was chosen such as to match the experiment distributions for the Reynolds stresses in the free-stream region. For the wall surfaces the boundary conditions are $u = v = k = 0$, for the ε concerning the linear eddy-viscosity model, $\varepsilon_w = 2\nu k_1/y_1^2$ where the subscript *1* stands for the first node close to the wall. For the non-linear model we used, $\varepsilon_w = 0$. For the k–ω equation we used $\omega \to 6\nu/(\beta_0 y^2)$ as $y \to 0$. Wilcox's suggestion to have at least five nodes with $y^+ < 2.5$ for stable computations and accurate results was also adopted. This boundary condition is applied to all these points and not only to the first point near the wall. A typical range for y^+ at the first computational node was 0.1–1 for the three models. For the pressure at the walls and for all the values at exit, $\partial \Phi/\partial n = 0$ was used, where stands for the solved variables and n for the normal to the boundary direction. Finally, a connection-matching condition was imposed for the cells that formed the O-type connection (south–north connection) into the grid, following the suggestions of Ferzinger and Peric (1999).

6. Results and discussion

The three models were applied for both experimental cases. In general, the linear k–ε model converged very fast and it needed about half iterations of the k–ω model to achieve convergence. The non-linear model needed the largest number of iterations. For the latter, the computational procedure was based on some preliminary iterations using the version of the linear low Reynolds Launder–Sharma model followed by a switch to the non-linear model. Based on the evolution of the measured free-stream Reynolds stresses, computer experiments led to the use in the final runs for the dissipation rate length scale a value of $l_\varepsilon = 20$ mm when uniform velocity distribution was imposed at inlet and 19 mm when mean shear was present. For this case, during the preliminary runs, a steep rise of the turbulent properties downstream the flow and in the free-stream region towards the exit was observed. The Reynolds stresses were growing in a monotonic way but this growth had a larger gradient than the measured one. This observation led to introducing of the vortex stretching parameter $7/(3\sqrt{15})c_{\varepsilon 3}\varepsilon^{1.5}$ in the ε-equation (and in a straightforward appropriate manner in the ω-equation), as defined by Bernard and Speziale (1992), with $c_{\varepsilon 1} = 0.01$. This inclusion led to a smoother monotonic growth. Fig. 17 shows the calculated downstream evolution of Reynolds stresses in the free-stream region for both cases using the non-linear model.

Fig. 18 shows two vector plots of the predicted flow fields (using the linear k–ε model) near the stagnation point and the flat plate's surface for both cases. The separated flow is clearly shown and also the differences in the longitudinal and normal directions when the mean shear is present. The last, gives a smaller recirculation zone in both directions.

For the uniform inlet mean velocity distribution, the velocity profiles at various stations for the three models compared with the experimental data are shown in Fig. 19. All the three models predict a region of separation a the joining of the curved leading edge with the flat horizontal surface. Experimental measurements could not identify this region due to the limitations of the hot-wire probe geometry, but plotting the experimental data against the numerical ones and by examining the velocity profile inside the boundary layer one can see that also the measurements give an indication of flow separation. The linear k–ε model has a very good agreement of the velocity distributions for all the stations, while the k–ε model predicts a larger recirculation region. On the

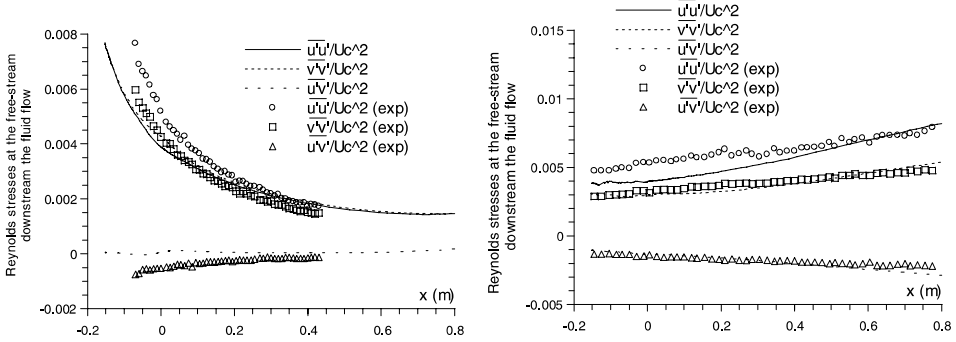

Fig. 17. Downstream evolution of $\overline{u'u'}$, $\overline{v'v'}$ and $\overline{u'v'}$ in the free-stream region for uniform inlet velocity distribution (left) and mean shear velocity distribution (right).

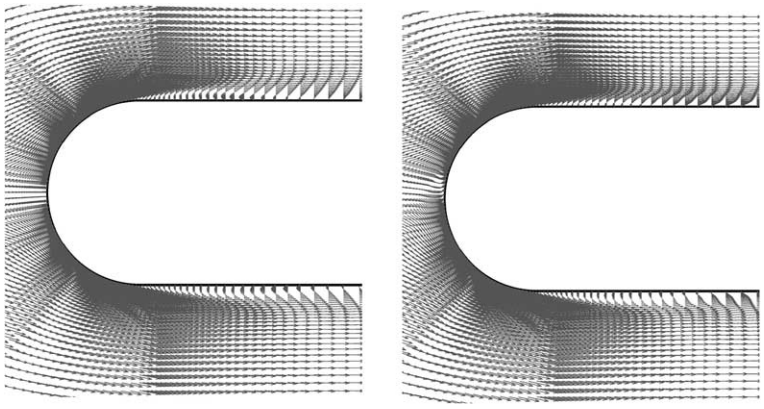

Fig. 18. Vector plot near the stagnation point and recirculation zone Uniform mean inlet velocity distribution (left), Mean shear inlet velocity distribution (right).

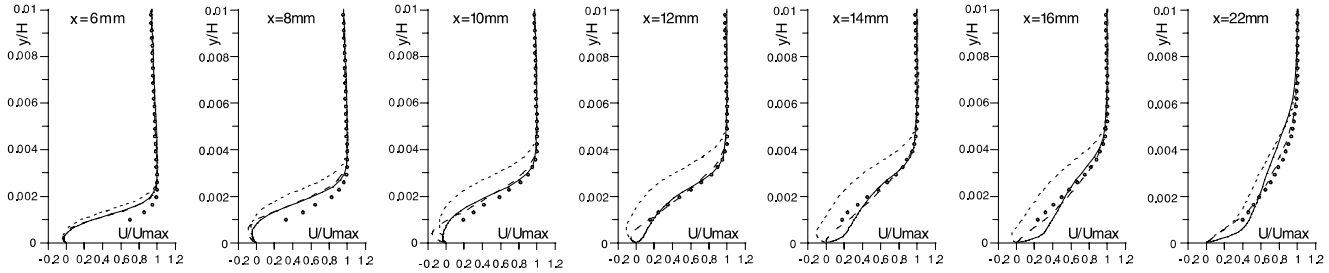

Fig. 19. Uniform mean inlet velocity distribution. Velocity profiles for 8 stations. Experiment: (•), linear k–ε: (- - -), non-linear k–ε: (—), linear k–ω: (· · ·).

other hand, the non-linear k–ε model predicts a smaller distance of the reattachment point, which lies between the two linear models, and also a smaller thickness for the separation region.

For the case where mean shear is present, Fig. 20 shows the velocity profiles against experimental data. The computed reattachment point for the two linear models differs by 1 mm. Among the two linear models, the k–ε model with the Abe et al. low Reynolds number modifications gives better predictions in all stations, while the k–ω model predicts a larger thickness of the separation bubble and thus, a larger recirculation length. This behavior of k–ω model, which was also observed in the case for uniform mean velocity distribution, gave us once more the indication that the model's closure constants need further calibration. In the past, Peng et al. (1997), have shown that the early version of the k–ω model of Wilcox (1994) overestimated the reattachment length in separated flows and they proposed new modifications concerning the damping functions for the viscous sublayer. It seems that the new version of k–ω model, as it was introduced by Wilcox in 1998, has the same behavior and thus it needs a more detailed development. The non-linear model k–ε model gives better results among all the tested models in the region where the boundary layer is separated but it predicts a smaller recirculation zone since the reattachment point is now located in about 2 mm upstream the measured one.

A logical explanation for this behaviour should be the excessive values of longitudinal values predicted by this model as it will be shown next. The distributions of the normal Reynolds stresses in the longitudinal direction, $\overline{u'u'}$ are shown in Figs. 21 and 22 for the uniform inlet velocity distribution and mean shear inlet velocity distribution respectively. The superiority of the non-linear model is clear when shear is present. The model predicts exactly the stress profiles inside the boundary layer and in the recirculation zone. The problems start when the flow was reattached and an overestimation occurs. In the case when shear is not present, there is an overestimation of the $\overline{u'u'}$ values in regions both inside and outside the recirculation zone. This tendency for both cases of the non-linear model for an overestimation is clearer near and beyond the reattachment point. This overestimation of the predicted near wall turbulence by the two equation non-linear model has been also reported by Chen et al. (1998b) for flows where an adverse pressure gradient is imposed and it can be characterized as a disadvantage of the model. The linear models

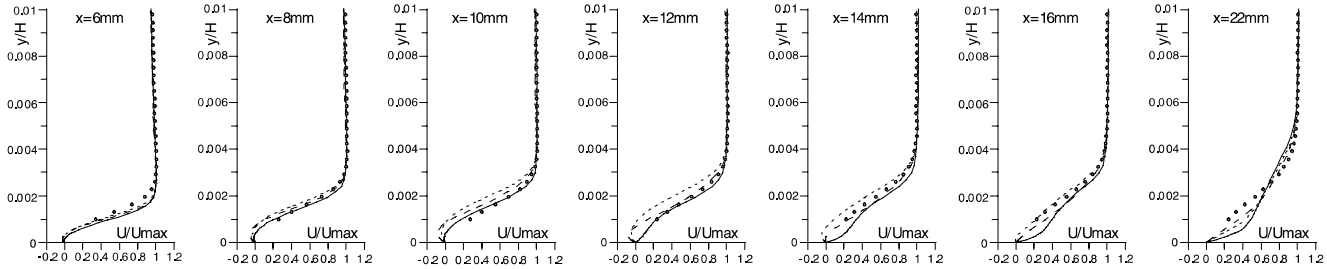

Fig. 20. Mean shear inlet velocity distribution. Velocity profiles for eight stations. Experiment: (•), linear k–ε: (- - -), non-linear k–ε: (—), linear k–ω: (· · ·).

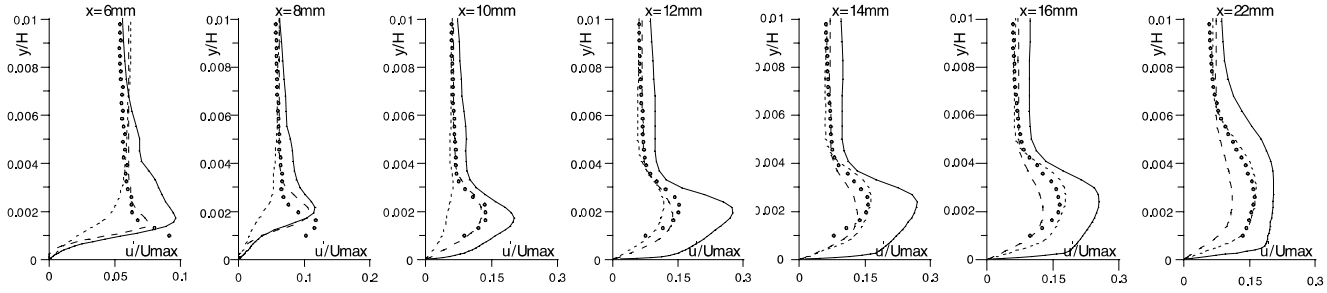

Fig. 21. Uniform mean inlet velocity distribution. Longitudinal Reynolds stresses. Experiment: (•), linear k–ε: (- - -), non-linear k–ε: (—), linear k–ω: (· · ·).

predict quite well the longitudinal stresses but this is mostly related to the isotropy of the calculated stresses.

Despite the limitations of the measurement technique since a single hot-wire inside the boundary layer was used, and so, the computed experimental integral parameters are based on extrapolations, one can see how the models behave. Fig. 23 shows the plots for the calculated boundary layer integral parameters against the experimental data. The aim of this part of the work was mainly to give an indication of how the three turbulence models behave for the two investigated flows.

In general, the two k–ε models give the best results while the k–ω model fails to capture in both cases the experimental data. In more details, the linear k–ε model with the Abe et al. low Reynolds modifications predicts in a satisfactory way the boundary layer integral parameters for the first experimental case, while the non-linear two equation k–ε model gives the best predictions when mean shear is present.

7. Conclusions

An experimental and computational work of the flow over a flat plate with a semi-circular leading edge and particularly in the region of transition was presented. This investigation is defined as the T3L test case initiated by the ERCOFTAC SIG for transition with the addition of an extra free-stream condition, i.e., the presence of a mean shear. The flow was examined using two inlet velocity distributions. One with a uniform velocity profile and another one with a free mean shear with $\partial\overline{U}/\partial y = 27.7\ \mathrm{s}^{-1}$. Both inlet profiles had $U_c = 5$ m/s for the center-line velocity.

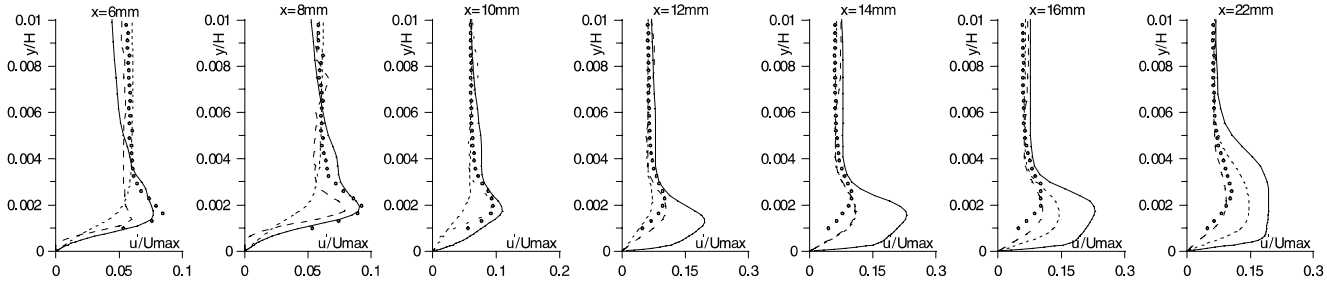

Fig. 22. Mean shear inlet velocity distribution. Longitudinal Reynolds stresses. Experiment: (•), linear k–ε: (- - -), non-linear k–ε: (—), linear k–ω: (· · ·).

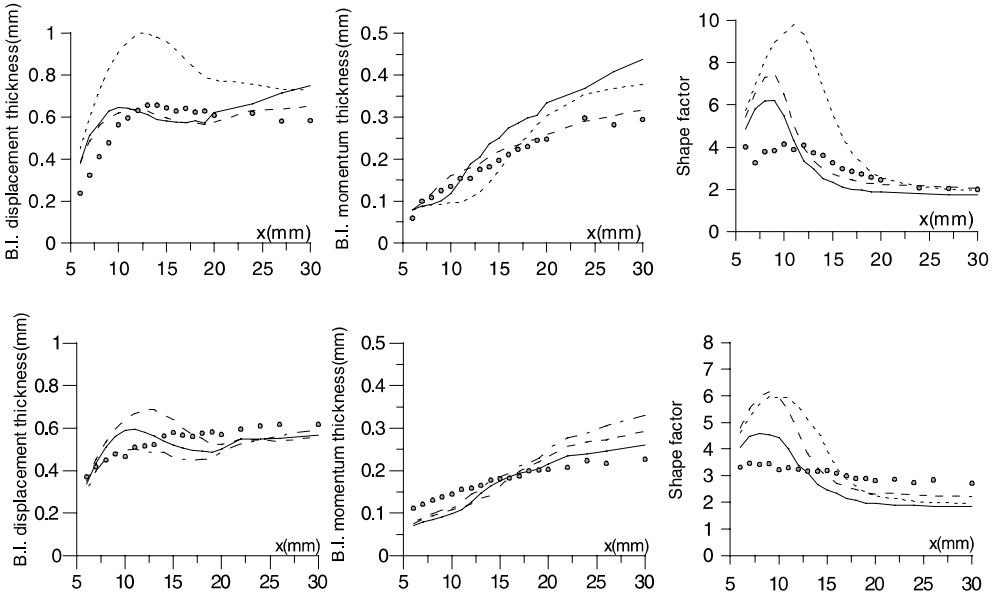

Fig. 23. Boundary layer integral parameters. Uniform mean inlet velocity (upper), mean shear inlet velocity distribution (lower) Experiment: (•), linear k–ε: (- - -), non-linear k–ε: (—), linear k– ω: (· · ·).

For both experiments, the separation of flow starts at a distance $x = 6$ mm from the leading edge. This distance is located in the region where the semi-circular leading edge blends with the horizontal surface of the flat plate. It was found that the existence of mean shear inlet velocity distribution affects the size of recirculation zone above and beyond the effect of FST alone. When mean shear is present, the separation region has smaller longitudinal length and thickness than the one with a uniform mean velocity inlet distribution. The question posed is which effect is responsible for this, the anisotropy in the Reynolds stresses or the mean shear itself. The present data cannot answer this and further work is needed. Detailed investigation of the experimental results showed also that for both cases and for the last measurement station far downstream, the flow is not completely turbulent. This is confirmed by the comparisons of the velocity distributions with typical turbulent profiles and by the experimental shape factor for the boundary layer. The last does not reach for both cases the typical value for turbulent flow of 1.3–1.4.

In order to obtain a more detailed picture of the flow, since the limitations introduced by the measurement techniques could not give a full one, a numerical study has been carried out using an elliptic Navier–Stokes solver. Three turbulence models were used. The aim was not the calibration of the models, since in the majority of the industrial applications of CFD, the available models are taken in their classical form. The models were introduced "as they are" and tested in order to evaluate their behavior with no other modifications. The first two models are based on the Boussinesq's linear approach for the eddy-viscosity. The extra equation solved in parallel with the k transport equation is either the transport of dissipation of turbulence or the transport of specific dissipation rate of turbulence ω. The third model is based on a non-linear form for the eddy-viscosity after Craft et al. that solves the two equations for the turbulence closure, k and ε. Regarding the velocity distributions the two k–ε models were found to give satisfactory results for both cases while the k–ω model predicted larger recirculation regions. When shear was present, the introduction of a vortex stretching parameter, as defined by Bernard and Speziale, was needed in order to diminish the steep rise of the Reynolds stresses downstream the fluid flow that were found to increase beyond the measured ones in the experiment. The non-linear model gave the better predictions concerning the longitudinal normal Reynolds stresses in the near wall region inside the recirculation zone, thought it overpredicted their values in regions outside the reverse flow region.

References

Abe, K., Kondoh, T., Nagano, Y., 1994. A new turbulence model for predicting fluid flow and heat transfer in separating and reattaching flows-I. Flow field calculations. Int. J. Heat Mass Transfer. 37, 139–151.

AUTh-group, 1994. Data on T3L test case, BRITE-EURAM Aero-CT92-0052 project.

Baines, W.D., Peterson, E.G., 1951. An investigation of flow through screens. ASME Trans. 73 (5), 467–480.

Bernard, P.S., Speziale, C., 1992. Bounded energy states in homogeneous turbulent shear flow—an alternative view. J. Fluid Eng. 114, 29–39.

Blair, M.F., 1982. Influence of free-stream turbulence on boundary layer transition in favorable pressure gradients. ASME Trans. J. Eng. Power 14, 743–750.

Bradshaw, P., 1971. An introduction to turbulence and its measurement. Pergamon Press Ltd.

Champagne, F.H., Harris, V.G., Corrsin, S., 1970. Experiments on nearly homogeneous turbulent shear flow. J. Fluid Mech. 41 (1), 81–139.

Chen, W.L., Lien, F.S., Leschziner, M.A., 1998a. Non-linear eddy-viscosity modeling of transitional boundary layers pertinent to turbomachine aerodynamics. Int. J. Heat Fluid Flow 19, 297–306.

Chen, W.L., Lien, F.S., Leschziner, M.A., 1998b. Computational prediction of flow around highly loaded compressor-cascade blades with non-linear eddy-viscosity models. Int. J. Heat Fluid Flow 19, 307–319.

Craft, T.J., Launder, B.E., Suga, K., 1997. Prediction of turbulent transitional phenomena with a nonlinear eddy-viscosity model. Int. J. Heat Fluid Flow 18, 15–28.

Coupland, J., Brierley, D.H., 1996. Transition in Turbomachinery Flows, Final Report. BRITE-EURAM Aero-CT92-0050 project. Rolls-Royce Plc.

Ellsworth, R.H., Mueller, T.J., 1991. Airfoil boundary layer measurements at low Reynolds in an accelerating flow from a nonzero velocity. Exp. Fluids 11, 368–374.

Ferziger, J.H., Peric, M., 1999. In: Computational Methods for Fluid Dynamics, 2nd ed. Springer, pp. 233–236.

Hall, D.J., Gibbings, J.C., 1972. Influence of stream turbulence and pressure gradient upon boundary layer transition. J. Mech. Eng. Div. 14 (2), 134–136.

Harris, V.G., Graham, A.H., Corrsin, S., 1977. Further experiments in nearly homogeneous turbulent shear flow. J. Fluid Mech. 81, 657–687.

Kato, M., Launder, B.E., 1993. The modeling of turbulent flow around stationary and vibrating square cylinder. 9th Symposium on Turbulent Shear Flows, Kyoto, 10-4-1 10-4-6.

Lage, C.F., Durst, F., Breuer, M., 1999. Wall effects on heat losses from hot-wires. Int. J. Heat Fluid Flow 20, 34–47.

Majumdar, S., 1988. Role of underrelaxation in momentum interpolation for calculation of flow with non-staggered grids. Num. Heat Transfer 13, 125–132.

Mayle, R.E., 1991. The role of laminar-turbulent transition in gas turbine engine. ASME Gas Turbine Conference 91-GT-261.

Murlis, J., Tsai, H.M., Bradshaw, P., 1982. The structures of turbulent boundary layer at low Reynolds numbers. J. Fluid Mech. 122, 13–56.

Musker, A.J., 1979. Explicit expression for the smooth wall velocity distribution in a turbulent boundary layer. AIAA J. 17 (6), 655–657.

Peng, S-H., Davidson, L., Holmberg, S., 1997. A modified low Reynolds number k–ω model for recirculating flows. J. Fluids Eng. 119, 867–875.

Rhie, C.M., Chow, W.L., 1983. A numerical study of the turbulent flow past an isolated airfoil with trailing edge separation. AIAA J. 21, 1525–1532.

Rohr, J.J., Itsweire, E.C., Helland, K.N., Van Atta, C.W., 1988. An investigation of the growth of turbulence in a uniform mean-shear flow. J. Fluid Mech. 187, 1–33.

Savill, A.M., 1995. A summary report on the COST ERCOFTAC Transition SIG Project evaluating turbulence models for predicting transition. ERCOFTAC Bulletin 24, 57–61.

Tavoularis, S., Corrsin, S., 1981. Experiments in nearly homogeneous turbulent shear flow with a uniform mean temperature gradient. Part 1. J. Fluid Mech. 104, 311–347.

Tennekes, H., Lumley, J.L., 1985. A first course in turbulence. MIT press 10th printing.

Tsuchiya, M., Murakami, S., Mochida, A., Kondo, K., Ishida, Y., 1997. Development of a new k–ε model for flow and pressure fields around bluff body. J. Wind Eng. Ind. Aerodyn. 67&68, 169–182.

Van Driest, E.R., Blumer, C.B., 1963. Boundary layer transition: free-stream turbulence and pressure gradient effects. AIAA J. 1 (6), 1303–1306.

Voke, P.R., Yang, Z., 1995. Numerical simulation of transition in a separation bubble. ERCOFTAC Bull. 24, 54–57.

VUB Group, Hazarika, B.K., Hirsch, Ch., 1992. Transition in turbomachinery flows. Final Report. BRITE-EURAM Aero-C(TT) project. Department of Fluid Mechanics, Vrije University Belgium.

Wilcox, D.C., 1994. Simulation of transition with a two-equation turbulence model. AIAA J. 32, 247–255.

Wilcox, D.C., 1998. Turbulence Modeling for CFD, 2nd ed., 2000. DCW Industries, Inc, Palm Drive, La Canada, California, USA, pp. 492–495.

Yakinthos, K., Goulas, A., 1995. The prediction of flow on a flat plate with a circular leading edge. 6th International Symposium on Computational Fluid Dynamics, Nevada III, 1407–1414.

Yakinthos, K., Goulas, A., 1999. The prediction of flow on a flat flate with a circular leading edge under zero and non-zero pressure gradient. 3rd European Conference on Turbomachinery: Fluid Dynamics and Thermodynamics IMechE, London, A, pp. 135–146.

Yakinthos, K., Tamamidis, P., Goulas, A., 1995. Calculation of steady incompressible flows using high-resolution monotonic schemes. In: Sixth International Symposium on Computational Fluid Dynamics. Nevada, III, pp. 1415–1422.

Zhu, J., 1991. A low diffusive and oscillation free convection scheme. Comm. Appl. Num. Meth., 7.